Autonomous circular heat engine

Giuliano Benenti,[1, 2, 3] Giulio Casati,[1, 4] Fabio Marchesoni,[5, 6] and Jiao Wang[7, 8]

[1]*Dipartimento di Scienza e Alta Tecnologia, Center for Nonlinear and Complex Systems, Università degli Studi dell'Insubria, via Valleggio 11, 22100 Como, Italy*
[2]*Istituto Nazionale di Fisica Nucleare, Sezione di Milano, via Celoria 16, 20133 Milano, Italy*
[3]*NEST, Istituto Nanoscienze-CNR, I-56126 Pisa, Italy*
[4]*International Institute of Physics, Federal University of Rio Grande do Norte, Campus Universitário - Lagoa Nova, CP. 1613, Natal, Rio Grande Do Norte 59078-970, Brazil*
[5]*Department of Physics, University of Camerino, 61032 Camerino, Italy*
[6]*Center for Phononics and Thermal Energy Science, School of Physics Science and Engineering, Tongji University, Shanghai 200092, China*
[7]*Department of Physics and Key Laboratory of Low Dimensional Condensed Matter Physics (Department of Education of Fujian Province), Xiamen University, Xiamen 361005, Fujian, China*
[8]*Lanzhou Center for Theoretical Physics, Lanzhou University, Lanzhou 730000, Gansu, China*

A dynamical model of a highly efficient heat engine is proposed, where an applied temperature difference maintains the motion of particles around the circuit consisting of two asymmetric narrow channels, in one of which the current flows against the applied thermodynamic forces. Numerical simulations and linear-response analysis suggest that, in the absence of frictional losses, the Carnot efficiency can be achieved in the thermodynamic limit.

I. INTRODUCTION

In the past decades, studying classical and quantum transport from the microscopic dynamics perspective has led to major advances in our understanding of heat conduction in low-dimensional systems [1–8], unveiling fundamental mechanisms of normal and anomalous transport and the conditions for heat rectification. In more recent years, investigations have been extended to more complicated situations involving two or more coupled currents, like in thermoelectric [9] or thermodiffusive [10] transport. Also in this case, a microscopic approach has played a unique role, finding new paths to achieve the Carnot efficiency in heat-to-work conversion [11, 12], extending Onsager reciprocal relations to systems with broken time-reversal symmetry [13, 14], and discovering the highly counterintuitive phenomenon of inverse currents, whereby an induced current flows opposite to the applied thermodynamic forces [15–17].

We propose to extend these notions to mass transport in low dimensional geometries, like narrow channels, where particles tend to move in single-files [18]. Indeed, when their diameter is comparable to the channel cross section, particles either do not pass each other at all, or do so only by overcoming a repulsive potential barrier and, possibly, at the cost of frictional losses [19]. However, single files subject to thermal gradient not only pose a fundamental problem for themselves (with potential applications to natural and artificial nano-devices [18]) but can also be suitably arranged to produce coupled particle currents.

Here, we demonstrate the possibility of building a circular heat engine consisting of two channels coupled to two particle reservoirs maintained at different temperatures. In addition, each channel contains particles of a different species, which either repel or bypass the particle flowing between the reservoirs, depending on their masses and velocities. For an appropriate choice of these parameters, the particle current in one channel may flow from low to high temperatures, and a stationary circular current between the reservoirs is established. As a consequence, the engine can convert a substantial fraction of the heat flowing from the hot to the cold reservoir into work. Extensive numerical simulations and a linear-response analysis suggest that the Carnot efficiency can indeed be achieved in the thermodynamic limit, i.e., for infinitely long channels.

II. MODEL AND ENGINE MECHANISM

A sketch of the proposed engine is plotted in Fig. 1. It is made of two one-dimensional (1D) channels of length L_Ξ ($\Xi = A, B$), coupled at their end points to two reservoirs of temperatures T_k ($k = L, R$). The number of particles in the overall system (channels plus reservoirs) is fixed. Each channel contains two species of particles, graphically represented by bullets of mass m and rods of mass M_Ξ, respectively. Dynamics inside the channels is purely Hamiltonian. All particles move freely, except when they collide with one another or hit a channel end point. When two particles collide, they either pass through each other, if their total energy in the frame of their center of mass is larger than a fixed inner potential barrier h_Ξ or simply bounce back; in both cases the pair momentum and the pair kinetic energy are conserved. The particle dynamics adopted here is inspired to well-known models for single-file diffusion and granular fluids, where h_Ξ can be regarded as the energy barriers associated with the configurational changes two particles undergo whereas passing each other in the channel [18, 20, 21]. For the engine to work it is essential that the rods in the two channels are different. When a rod hits a channel-reservoir boundary, it is reflected
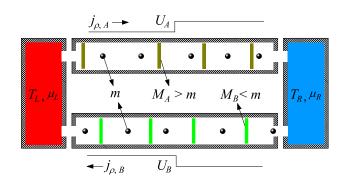
FIG. 1: Sketch of a two-channel engine working between two reservoirs of fixed temperatures T_L and T_R and adjustable chemical potentials μ_L and μ_R. The two particle species in each channel are represented by bullets of mass m and rods of mass $M_{A,B}$. When a stationary circular current of bullets is established, the engine can work against applied potentials $U_{A,B}$. In this drawing, the channels have equal lengths, $L_A = L_B$.

back with a newly assigned velocity sampled from a certain distribution determined by the reservoir temperature (see below). Accordingly, the number of rods in each channel is conserved, as they only exchange energy with the reservoirs. As for the bullets, when one reaches a channel boundary, it will enter the connected reservoir. Meanwhile, the reservoirs keep injecting bullets into the channels with rates and energy distributions determined by their temperatures T_k and densities (or chemical potentials μ_k). Following these simple rules, after an appropriate transient, a steady-state circular current of bullets sets in, sustained by the temperature difference imposed by the reservoirs; the bullet densities (and the chemical potentials μ_k) in each (large but finite) reservoir autonomously adjust to support such a current. Ultimately, the circulating particle current and, thus, the possibility of extracting useful work depend on the fixed temperature difference between the reservoirs.

Suppose that $T_L > T_R$ and $\mu_L > \mu_R$. Intuitively, we may expect that in each channel, both the energy and the bullet current would flow forward from left to right. This is indeed the case when $M_\Xi > m$. In sharp contrast, for $M_\Xi < m$, either the energy or the bullet current – depending on the parameter choice – may flow on reverse from right to left, against both thermodynamical forces [16]. The mechanism of current reversal is related to the fact that under the given collision rules, the probability for a bullet-rod pair to cross each other is higher when the light (heavy) particle is on the hot (cold) reservoir side because in such a case, their relative velocities are likely to be higher. The kinetics of bullets and rods, thus, causes a left-right unbalance in their densities along the channel [22].

Thanks to this peculiar dynamical effect, we can make the bullets flow on reverse in one channel, say, channel B, by setting $M_B < m$ and, thus, create a clockwise circular bullet current through the whole system. Such current

can work also against an external bias, represented by the potentials $U_{A,B}$ in Fig. 1 [23]. For instance, one could use part of the kinetic energy of the circulating particles to lift a weight. A fraction of the heat flowing from the hot to the cold reservoir would be then converted into mechanical work, the rest being dumped into the cold reservoir. This fulfills the function of an engine.

III. LINEAR RESPONSE ANALYSIS

Before presenting the output of our numerical simulations, we analyze the model in the linear-response regime. We adopt here for concreteness the language of thermoelectricity, with charged particles circulating, such as in a thermocouple, but our results apply equally well to other coupled flows, such as in thermodiffusion. We start from the linear transport equations [24, 25] for channel Ξ ($\Xi = A, B$),

$$\begin{pmatrix} J_\Xi^\rho \\ J_\Xi^u \end{pmatrix} = \begin{pmatrix} \mathcal{L}_\Xi^{\rho\rho} & \mathcal{L}_\Xi^{\rho u} \\ \mathcal{L}_\Xi^{\bar{u}\rho} & \mathcal{L}_\Xi^{\bar{u}u} \end{pmatrix} \begin{pmatrix} \mathcal{F}_\Xi^\rho/L_\Xi \\ \mathcal{F}^u/L_\Xi \end{pmatrix}. \qquad (1)$$

Here J_Ξ^ρ and J_Ξ^u are the particle (bullet) and the energy currents, $\mathbb{L}_\Xi = (\mathcal{L}_\Xi^{ij})$ $(i, j = \rho, u)$ the matrix of the Onsager kinetic coefficients, and $\mathcal{F}_\Xi^\rho$ and $\mathcal{F}^u$ the thermodynamical forces, defined as $\mathcal{F}_A^\rho = \mu_L\beta_L - (\mu_R + U_A)\beta_R$, $\mathcal{F}_B^\rho = \mu_L\beta_L - (\mu_R - U_B)\beta_R$, and $\mathcal{F}^u = \beta_R - \beta_L$, respectively, with $\beta_k = 1/(k_B T_k)$ $(k = L, R, k_B$ is the Boltzmann constant). The Onsager coefficients are related with the familiar transport coefficients, i.e., the electrical conductivity σ_Ξ, the thermal conductivity κ_Ξ, and the thermopower S_Ξ, as follows:

$$\sigma_\Xi = \frac{e^2}{T} L_\Xi^{\rho\rho}, \ \ \kappa_\Xi = \frac{1}{T^2} \frac{\det \mathbb{L}_\Xi}{L_\Xi^{\rho\rho}}, \ \ S_\Xi = \frac{1}{eT} \left(\frac{L_\Xi^{\rho u}}{L_\Xi^{\rho\rho}} - \mu \right),$$
$$(2)$$

where e is the charge of each particle, $T \approx T_L \approx T_R$, $\mu \approx \mu_L \approx \mu_R$ in linear response approximation. We can then rewrite Eq. (1) as

$$\begin{cases} L_A J_A^u = \kappa_A' \Delta T + T\sigma_A S_A(\Delta\mu - U_A), \\ L_B J_B^u = \kappa_B' \Delta T + T\sigma_B S_B(\Delta\mu + U_B), \\ L_A J_A^\rho = \sigma_A S_A \Delta T + \sigma_A(\Delta\mu - U_A), \\ L_B J_B^\rho = \sigma_B S_B \Delta T + \sigma_B(\Delta\mu + U_B). \end{cases}$$

Here $\kappa_A' = \kappa_A + T\sigma_A S_A^2$, $\kappa_B' = \kappa_B + T\sigma_B S_B^2$, $\Delta T = T_L - T_R$, and $\Delta\mu = \mu_L - \mu_R$. On imposing the circular, steady-flow condition

$$J_A^\rho + J_B^\rho = 0, \qquad (3)$$

the output power P and the efficiency η read respectively

$$P = J_A^\rho U_A - J_B^\rho U_B, \ \ \eta = P/(J_A^u + J_B^u). \qquad (4)$$

Note that by using the steady-flow condition, P and η can be explicitly rewritten as functions of $U_A + U_B$, rather than of U_A and U_B, separately (see Appendix A).

Moreover, both the maximum efficiency $\eta_{\max}$ and the efficiency at the maximum power $\eta(P_{\max})$ have the usual dependence [9] on a nondimensional figure of merit,

$$YT = \frac{(\sigma_A/L_A)(\sigma_B/L_B)(S_A - S_B)^2}{(\sigma_A/L_A + \sigma_B/L_B)(\kappa_A/L_A + \kappa_B/L_B)} T, \quad (5)$$

(in lieu of the thermoelectric figure of merit ZT [26, 27]), namely

$$\eta_{\max} = \eta_C \frac{\sqrt{YT+1}-1}{\sqrt{YT+1}+1}, \quad \eta(P_{\max}) = \frac{\eta_C}{2}\frac{YT}{YT+2}, \quad (6)$$

with Carnot efficiency $\eta_C = 1 - T_R/T_L$ (we assume $T_L > T_R$) and maximum power

$$P_{\max} = \frac{1}{4}\frac{\sigma_A\sigma_B}{\sigma_A L_B + \sigma_B L_A}(S_A - S_B)^2(\Delta T)^2.$$

The power-efficiency trade-off for a given value of YT can also be obtained (see, e.g., Ref. [9]),

$$\frac{\eta}{\eta_C} = \frac{P/P_{\max}}{2[1 + 2/(YT) \mp \sqrt{1 - P/P_{\max}}\,]}. \quad (7)$$

A limiting case is represented by the conventional thermocouple configuration with $L_A = L_B \equiv L$, $\sigma_A = \sigma_B \equiv \sigma$, $\kappa_A = \kappa_B \equiv \kappa$, and $S_A = -S_B \equiv S$. Here, the figure of merit ZT is recovered, $ZT = YT$, and the maximum power, $P_{\max} = (\sigma/2L)S^2(\Delta T)^2$, amounts to twice the maximum power of a single channel.

IV. NUMERICAL STUDY

Our numerical results show that the proposed engine is very efficient. In our simulations, we model the reservoirs as 1D ideal gases of bullets [28]. They inject bullets into the channels randomly in time, with constant rates γ_k ($k = L, R$) [29], $\gamma_k = (\rho_0/\sqrt{2\pi m\beta_0})(\beta_0/\beta_k)e^{\mu_k\beta_k - \mu_0\beta_0}$, where $T_0 = 1/(k_B\beta_0)$, ρ_0, and μ_0 are, respectively, the temperature, particle number density, and chemical potential of a reference state (see below). The injection intervals thus follow the Poisson distribution $\pi_k(t) = \gamma_k e^{-\gamma_k t}$, whereas the speeds of the injected particles are sampled according to the Maxwell distribution [30], $P_k(v, m) = m|v|\beta_k e^{-mv^2\beta_k/2}$. Accordingly, when a rod particle of mass M_Ξ hits the channel boundary next to reservoir k, it bounces back with speed distribution $P_k(v, M_\Xi)$.

To establish the circular, steady-flow condition of Eq. (3), rather than simulating the entire closed system (that is, channels and reservoirs), we simulated first the two channels, separately, and computed the two curves J^ρ_Ξ vs U_Ξ ($\Xi = A, B$). Then, for a given value of $J^\rho \equiv J^\rho_A = -J^\rho_B$, we determined the corresponding values of $U_{A,B}$, to be used in the subsequent simulation steps, which involve both channels simultaneously. After
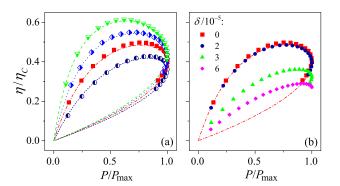

FIG. 2: (a) Efficiency, η, vs output power P for two channels of equal length $L_A = L_B$. Blue dots, red squares, blue diamonds, and green triangles are for $L_\Xi = 100, 200, 400,$ and 1600, respectively. The curves next to each data set are obtained via Eq. (7) with numerically computed YT. Fixed model parameters are as follows: $h_A = h_B = 1$, $M_A = 1.5$, $M_B = 0.5$, $T = 1$, and $\mu = 1.5$; Other tunable parameters are $\Delta T = 0.1$ and $\Delta\mu = 0.15$. (b) η vs P, such as in (a), for $L_\Xi = 200$ but finite dissipation parameter δ (see text below).

the system had relaxed to its stationary state, we computed the time-averaged currents and from Eqs.(4), the relevant output power P and the efficiency η.

In the simulations reported here, we set $T_L = T + \Delta T/2$, $\mu_L = \mu + \Delta\mu/2$, $T_R = T - \Delta T/2$, and $\mu_R = \mu - \Delta\mu/2$. The number of rods in each channel is set to half of the expected particle number of a 1D ideal gas at the equilibrium with the assigned T and μ, i.e., $N_{rod,\Xi} = \rho L_\Xi/2$ with $\rho = \rho_0\sqrt{\beta_0/\beta}e^{\beta\mu - \beta_0\mu_0}$. As for the reference state, we set $\rho_0 = 1$, $T_0 = 1$, and $\mu_0 = 0$ (in units such that $m = 1$, $e = 1$, and $k_B = 1$). To make the system evolve in time, we implemented an effective event-driven algorithm [31], which yields output data points with relative error less than 0.5%.

Our data show that this model works as an autonomous engine in a wide range of parameters. Typical numerical results for the efficiency and the power are displayed in Fig. 2(a), where for any given system size $L_A = L_B$, a data point represents the result obtained for a certain value of J^ρ (or U_A and U_B). The closed curve next to each set of the data points is the prediction of Eq. (7), plotted for the corresponding value of YT, also obtained by numerical simulation as explained below. The linear-response theory reproduces quite closely the numerical data of Fig. 2(a). Moreover, such agreement improves with increasing the system size as expected since the temperature gradient $(\nabla T)_\Xi = \Delta T/L_\Xi$, decreases upon increasing L_Ξ at constant ΔT. More importantly, we notice that as L_Ξ increases, the efficiency versus power curves shift upwards, meaning that the engine performance improves. This remark hints at the possibility that the figure of merit YT in Eq. (7) is a monotonically increasing function of the system size.

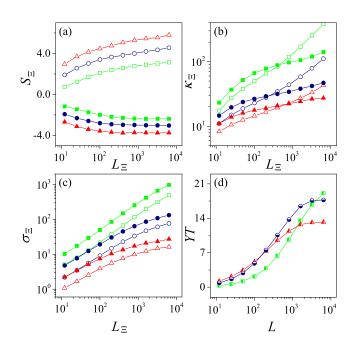To determine YT we made use of Eq. (5), where the transport coefficients are also to be computed numeri-

FIG. 3: (a)-(c) Transport coefficients of the two channels vs their lengths, where the empty and the full symbols are for channel A and channel B, respectively. (d) YT vs $L_A = L_B \equiv L$ for $h_A = h_B$. In all four panels, green squares, blue dots, and red triangles are for, respectively, $h_\Xi = 0.5$, 1.0, and 1.5, All other simulation parameters are the same as in Fig. 2(a).

cally. To this purpose, the two channels were considered separately. For each channel, we followed the method detailed in Ref. [29], i.e., the particle and energy currents were measured twice, namely, for $\mathcal{F}_\Xi^\rho \neq 0$ and $\mathcal{F}^u = 0$, and for $\mathcal{F}_\Xi^\rho = 0$ and $\mathcal{F}^u \neq 0$ (having set $U_\Xi = 0$). The Onsager kinetic coefficients can then be evaluated through Eq. (1). The corresponding transport coefficients, Eq. (2), computed for three different potential barrier values, $h_A = h_B = 0.5$, 1.0, and 1.5, are displayed in Figs. 3(a)-3(c) vs L_Ξ. First of all, we note that due to the inverse bullet current in channel B, the off-diagonal elements of the Onsager matrix are negative [16, 32]. Accordingly, the Seebeck coefficients S_A and S_B are, respectively, positive and negative [see Fig. 3(a)], which enhances the figure of merit YT through the quadratic factor $(S_A - S_B)^2$ in Eq. (5). This is the key advantage of our model. Moreover, due to the fact that the momentum is the only conserved mechanical quantity both S_Ξ and factor $(S_A - S_B)^2$ in our expression for YT are predicted to saturate in the thermodynamic limit [12], a prediction corroborated by our numerical simulations.

As for the electrical and thermal conductivities, it helps consider two limits for the potential barriers h_Ξ. In the limit $h_\Xi \to \infty$, all particles turn out to be hard core and the two species in each channel are always non-passing. The bullet currents are therefore blocked, thus resulting in $\sigma_\Xi = 0$. On the other hand, according to the 1D heat conduction theory [3, 4, 33, 34], in the thermo-

dynamical limit the heat conductivity would diverge, such as $\kappa_\Xi \sim L_\Xi^\nu$ with $0 < \nu < 1$. Consequently, see Eq. (5), in the same limit both YT and the engine efficiency would vanish. In the opposite limit $h_\Xi \to 0$ the dynamics becomes integrable and the bullets flow through the channel freely; hence, $\sigma_\Xi \sim L_\Xi$ and $\kappa_\Xi \sim L_\Xi$. This working regime is not advantageous, either. Indeed, the bullet-rod interaction is crucial to maintain an inverse current [16] in channel B. Therefore, when the bullet-rod interaction vanishes for $h_B \to 0$, so does the inverse current. More precisely, there exists a critical value h_B^*, such that for $h_B < h_B^*$, the bullet current in channel B starts flowing forward and our engine, thus, stops working. Note that $h_B^* \sim L_B^{-0.5}$ (see Appendix B) so that $h_B^* \to 0$ as $L_B \to \infty$. It is, therefore, reasonable to conjecture that for a given system size, one can determine the optimal finite values of h_Ξ that maximize YT.

Based on the data in Figs. 3(a)- 3(c), we can investigate how YT depends on the system size for assigned values of h_Ξ. We find that, in general, when $L_A + L_B$ is fixed, YT reaches its maximum for $L_A \simeq L_B$ and $h_A = h_B$. For this reason, we focus on cases with $L_A = L_B$ and $h_A = h_B$ and in Fig. 3(d) plot YT vs L_Ξ for three values of h_Ξ. YT is confirmed to be an increasing function of L_Ξ, which saturates asymptotically to a value that increases as h_Ξ decreases. In addition, the optimal h_Ξ value that, for a given L_Ξ, maximizes YT decreases as L_Ξ increases [from Fig. 3(d), we can tell that the optimal h_Ξ value is larger than one for $L_\Xi < 150$ but smaller than one for $L_\Xi > 4000$]. Based on the numerical and analytical results reported above, we conjecture that the engine achieves the Carnot efficiency (corresponding for $YT \to \infty$ to the values of bias potentials $U_{A,B}$ for which the efficiency is maximum, transport is dissipation-less and power vanishes [9]) in the thermodynamic limit $L_\Xi \to \infty$, and for vanishing barriers $h_\Xi \sim 1/\sqrt{L_\Xi} \to 0$.

Of course, this conclusion holds under the condition that the dynamics in both channels is frictionless. Two particles in a single file (say, a bullet and a rod) do squeeze their way past each other when their relative velocity $|v_{i+1} - v_i|$ is large enough to overcome the relevant repulsive barrier h_Ξ. However, the collisional mechanism may involve the loss of a fraction of their kinetic energy. Accordingly, imposing pair momentum conservation, the respective momentum changes would be $\Delta p_i = -\Delta p_{i+1} = \delta/(v_i - v_{i+1})$ with δ the assumed dissipation parameter. Such a simple collisional friction model impacts the backward current in channel B more than the forward current in channel A; this results in the net suppression of the power-efficiency performance of the engine illustrated in Fig. 2(b).

V. SUMMARY AND DISCUSSION

We have exploited the phenomenon of inverse particle current to design an autonomous engine, which for a given temperature difference, operates without any exter-
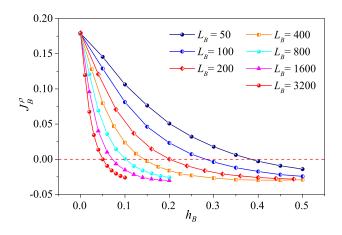
FIG. 4: Dependence of the current J_B^ρ on the potential barrier h_B for $M_B = 0.5$, $T = 1$, $\mu = 1.5$, $\Delta T = 0.1$, and $\Delta\mu = 0$.

nal time-dependent control. When operated on reverse, this engine would work as a refrigerator. The linear-response analysis outlined above shows that the engine performance would still be governed by YT with maximum efficiency as in Eq. (6) but with reversed Carnot coefficient $\eta_C = (T_L/T_R - 1)^{-1}$. Finally, due to its peculiar nature, distinct from the conventional steady-state engines characterized by ZT, our engine can be used to investigate the trade-off of power, efficiency, and fluctuations, encompassed in thermodynamic uncertainty relations [35–38].

Appendix A: Dependence of power and efficiency on $U_A + U_B$

Given the currents [see the four equations before Eq. (3)] and the steady-flow condition $J_A^\rho + J_B^\rho = 0$, we obtain

$$J_A^\rho = -J_B^\rho = \frac{1}{2}(J_A^\rho - J_B^\rho) = \frac{1}{2}\left[\left(\frac{\sigma_A S_A}{L_A} - \frac{\sigma_B S_B}{L_B}\right)\Delta T\right.$$

$$\left. + \left(\frac{\sigma_A}{L_A} - \frac{\sigma_B}{L_B}\right)\Delta\mu - (U_A + U_B)\right], \qquad (A1)$$

where the last equality is obtained by substituting J_A^ρ and J_B^ρ. This expression shows that both J_A^ρ and J_B^ρ de-

pend on $U_A + U_B$, rather than on U_A and U_B, separately. Moreover, as

$$P = J_A^\rho U_A - J_B^\rho U_B = J_A^\rho(U_A + U_B), \qquad (A2)$$

we conclude that the power depends on $U_A + U_B$ as well. On the other hand, by eliminating $\sigma_A(\Delta\mu - U_A)$ and $\sigma_B(\Delta\mu - U_B)$ based on the four equations before Eq. (3), we have that

$$\begin{cases} J_A^u = TS_A J_A^\rho + \kappa_A \Delta T/L_A, \\ J_B^u = TS_B J_B^\rho + \kappa_B \Delta T/L_B. \end{cases} \qquad (A3)$$

It follows that J_A^u and J_B^u, and, in turn, the efficiency, also depend on $U_A + U_B$ alone. In conclusion, as long as their sum is kept constant, we can vary U_A and U_B without modifying power and efficiency.

Appendix B: Critical value for the potential barrier

There exists a critical value h_B^*, such that for $h_B < h_B^*$, the bullet current in channel B starts flowing forward and the engine, thus, stops working. In the main text it was stated that $h_B^* \sim L_B^{-0.5}$. This is a very accurate numerical observation. Figure 4 shows the dependence of the particle current J_B^ρ on the potential barrier h_B for various channel lengths L_B. For a given value of L_B, the critical potential value h_B^* is identified by interpolating data points and solving $J_B^\rho(h_B^*) = 0$. We can see from Fig. 5 that the obtained values of the critical potential barrier are in excellent agreement with the scaling $h_B^* \sim L_B^\alpha$ with $\alpha = -0.500 \pm 0.004$.
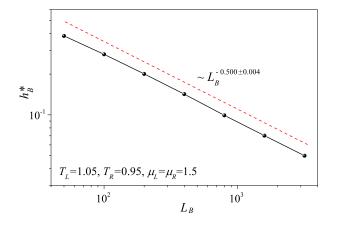

FIG. 5: Dependence of the critical potential barrier h_B^*, obtained from the data of Fig. 4, on the channel length L_B.

[1] G. Casati, J. Ford, F. Vivaldi, and W. M. Visscher, Phys. Rev. Lett. **52**, 1861 (1984).

[2] F. Bonetto, J. L. Lebowitz, and L. R. Bellet, in *Mathematical Physics 2000*, edited by A. Fokas, A. Grigoryan, T. Kibble, and B. Zegarlinski (Imperial College Press, London, 2000).

[3] S. Lepri, R. Livi, and A. Politi, Phys. Rep. **377**, 1 (2003).

[4] A. Dhar, Adv. Phys. **57**, 457 (2008).

[5] N. Li, J. Ren, L. Wang, G. Zhang, P. Hänggi, and B. Li, Rev. Mod. Phys. **84**, 1045 (2012).

[6] *Thermal transport in low dimensions: from statistical physics to nanoscale heat transfer*, edited by S. Lepri, Springer Lecture Notes in Physics Vol. No. 921 (Springer, Switzeland, 2016).

[7] G. Benenti, G. Casati, C. Mejía-Monasterio, and M. Peyrard, *From thermal rectifiers to thermoelectric devices* (Springer, Switzeland, 2016), in Ref. [6].

[8] G. Benenti, S. Lepri, and R. Livi, Front. Phys. **8**, 292 (2020).

[9] G. Benenti, G. Casati, K. Saito, and R. S. Whitney, Phys. Rep. **694**, 1 (2017).

[10] R. Piazza and A. Parola, J. Phys.: Condens, Matter **20**, 153102 (2008).

[11] R. Luo, G. Benenti, G. Casati, and J. Wang, Phys. Rev. Lett. **121**, 080602 (2018).

[12] G. Benenti, G. Casati, and J. Wang, Phys. Rev. Lett. **110**, 070604 (2013).

[13] S. Bonella, G. Ciccotti, and L. Rondoni, Europhys. Lett. **108**, 60004 (2014).

[14] R. Luo, G. Benenti, G. Casati, and J. Wang, Phys. Rev. Research **2**, 022009(R) (2020).

[15] J. Cividini, D. Mukamel, and H. A. Posch, J. Phys. A **51**, 085001 (2018).

[16] J. Wang, G. Casati, and G. Benenti, Phys. Rev. Lett. **124**, 110607 (2020).

[17] Y. Zhang and Z. Xie, Phys. Rev. E **104**, 064142 (2021).

[18] For a review, see A. Taloni, O. Flomenbom, R. Castañeda-Priego, and F. Marchesoni, Soft Matter **13**, 1096 (2017)

[19] K. K. Mon and J. K. Percus, J. Chem. Phys. **117**, 2289 (2002).

[20] J. Kärger, D .M Ruthven, and D. N Theodorou, *Diffusion in Nanoporous Materials* (Wiley-VCH, Weinheim, 2012).

[21] B. C. Bukowski *et al.* Adsorption **27**, 683 (2021).

[22] J. Wang and G. Casati, Phys. Rev. Lett. **118**, 040601 (2017).

[23] In our simulations, we applied the potentials to both species of particles. For convenience, we used step potentials.

[24] H. B. Callen, *Thermodynamics and an Introduction to Thermostatics*, 2nd ed. (Wiley, New York, 1985).

[25] S. R. de Groot and P. Mazur, *Nonequilibrium Thermodynamics* (North-Holland, Amsterdam, 1962).

[26] M. Horvat, T. Prosen, and G. Casati, Phys. Rev. E **80**, 010102(R) (2009).

[27] J. Wang, G. Casati, T. Prosen, and C.-H. Lai, Phys. Rev. E **80**, 031136 (2009).

[28] C. Mejía-Monasterio, H. Larralde, and F. Leyvraz, Phys. Rev. Lett. **86**, 5417 (2001); H. Larralde, F. Leyvraz, and C. Mejía-Monasterio, J. Stat. Phys. **113**, 197 (2003).

[29] K. Saito, G. Benenti, and G. Casati, Chem. Phys. **375**, 508 (2010).

[30] J. L. Lebowitz and H. Spohn, J. Stat. Phys. **19**, 633 (1978); R. Tehver, F. Toigo, J. Koplik, and J. R. Banavar, Phys. Rev. E **57**, R17 (1998).

[31] G. Casati and T. Prosen, Phys. Rev. E **67**, 015203(R) (2003).

[32] S. Iubini, S. Lepri, and A. Politi, Phys. Rev. E **86**, 011108 (2012).

[33] H. van Beijeren, Phys. Rev. Lett. **108**, 180601 (2012).

[34] C. B. Mendl and H. Spohn, Phys. Rev. Lett. **111**, 230601 (2013).

[35] A. C. Barato and U. Seifert, Phys. Rev. Lett. **114**, 158101 (2015).

[36] T. R. Gingrich, J. M. Horowitz, N. Perunov, and J. L. England, Phys. Rev. Lett. **116**, 120601 (2016).

[37] J. M. Horowitz and T. R. Gingrich, Nature Physics **16**, 15 (2020).

[38] P. Pietzonka and U. Seifert, Phys. Rev. Lett. **120**, 190602 (2018).